Fast and accurate calculation of EXAFS Debye-Waller factors in UO_2 using the dynamical matrix method

Nicholas Marcella,[1,2,*] Shuxiang Zhou,[3,*] Fernando D. Vila,[4] Nirmalendu Patra,[5] Alexei Kuzmin,[6] Dmitry S. Maltsev,[7,8] Alexander S. Ivanov,[9] Sheng Dai,[7,8] Ruchi Gakhar,[10] Kathy Dardenne,[11] Jörg Rothe,[11] Sebastian Couweleers,[12] Anna L. Smith,[12] Simerjeet K. Gill,[5] and Anatoly I. Frenkel[13,14,†]

[1]*Department of Geosciences, Stony Brook University, Stony Brook, New York 11794, USA*
[2]*Joint Photon Sciences Institute, Stony Brook University, Stony Brook, New York 11794, USA*
[3]*Department of Computational Mechanics and Materials, Idaho National Laboratory, Idaho Falls, Idaho 83415, USA*
[4]*Department of Physics, University of Washington, Seattle, Washington 98195, USA*
[5]*Nuclear Science and Technology Department, Brookhaven National Laboratory, Upton, New York 11973, USA*
[6]*Institute of Solid State Physics, University of Latvia, Kengaraga street 8, LV 1063 Riga, Latvia*
[7]*Chemical Sciences Division, Oak Ridge National Laboratory, Oak Ridge, Tennessee 37831, USA*
[8]*Department of Chemistry, Institute for Advanced Materials and Manufacturing, University of Tennessee, Knoxville, Tennessee 37996, USA*
[9]*Department of Nuclear Engineering, University of Tennessee, Knoxville, Tennessee 37996, USA*
[10]*Advanced Technology of Molten Salts Department, Idaho National Laboratory, Idaho Falls, Idaho 83415, USA*
[11]*Institute for Nuclear Waste Disposal (INE), Radionuclide Speciation Department, Karlsruhe Institute of Technology (KIT), Hermann-von-Helmholtz-Platz 1, 76344 Eggenstein-Leopoldshafen, Germany*
[12]*Radiation Science & Technology Department, Faculty of Applied Sciences, Delft University of Technology, Mekelweg 15, 2629JB Delft, Netherlands*
[13]*Department of Materials Science and Chemical Engineering, Stony Brook University, Stony Brook, New York 11794, USA*
[14]*Division of Chemistry, Brookhaven National Laboratory, Upton, New York 11973, USA*

(Received 17 February 2026; accepted 8 May 2026; published 8 June 2026; corrected 11 June 2026)

Theoretical modeling of bonding dynamics in metal oxides is required for predicting their thermal conductivity, catalytic activity, and mechanical properties. A primary challenge is the scarcity of experimental methods for validating theoretical predictions of these atomic-scale dynamics. This work presents a workflow that uses experimental extended x-ray absorption fine structure (EXAFS) data collected at high temperatures to validate an interatomic force field for uranium dioxide (UO_2), an important model material. The validated force field is then used to drive computationally intensive molecular dynamics (MD) simulations and as input for the much faster dynamical matrix Debye-Waller (DMDW) method. The predicted values of the Debye-Waller factors from the DMDW calculations are in good agreement with those obtained from the MD simulations, with residual pair-specific differences attributable to quantum zero-point motion at low temperatures and lattice anharmonicity at high temperatures. We further show that theoretical EXAFS spectra constructed directly from DMDW-derived Debye-Waller factors reproduce the experimental data (at relatively low temperatures) with accuracy comparable to full MD-EXAFS, providing an additional validation of the choice of the potential. This study establishes a validated, rapid computational pathway for modeling bond dynamics, naturally incorporating quantum nuclear statistics absent in classical simulations, which are essential for the mechanistic understanding of complex oxide materials.

DOI: 10.1103/l3lr-qhdz

I. INTRODUCTION

Metal-oxide functionalities—applied widely in fields from catalysis and energy conversion to sensing and electronics—are governed not just by static structure but by bond dynamics: how local coordination fluctuates, defects form/migrate, and phonons scatter carriers or mediate reactions. For example, at engineered oxide interfaces, bonding across dissimilar lattices can induce new phase formation and emergent behaviors absent in either bulk parent [1,2]. In heterogeneous catalysis, transition-metal oxides (TMOs) serve as supports and active phases whose surface bonding can be tuned chemically—e.g., by peroxide species [3] or structurally through aliovalent doping [4], where bond breaking and forming are key to controlling reactivity, such as in the water-gas shift reaction via metal-vacancy complex formation [4–6]. Bonding dynamics are equally central to environmental photocatalysis (e.g., dye [7,8] and antibiotic degradation [9,10]), photoelectrochemical water splitting [11–13], and selective sensing [14,15], where bulk and nanostructured oxides exploit defect- and size-dependent vibrational and electronic structure to drive reactions or selectively bind species [2–15]. Transport phenomena in conductive oxides (e.g., Magnéli-phase titania) and thermoelectric TMOs likewise depend on the interplay of

*These authors contributed equally to this work.
†Contact author: frenkel@bnl.gov

 ©2026 American Physical Society

lattice vibrations and carrier scattering [16,17]. Thus, in these and many other cases, the development of accurate predictive models of local bonding dynamics is essential for explaining their bulk properties and exploiting them for the design of materials with target functionalities.

Within this broader landscape, uranium dioxide (UO_2) is an attractive test bed for developing and validating such models, especially as a canonical nuclear fuel used in the current fleet of light-water reactors around the world, and a candidate for advanced power concepts (e.g., high-temperature gas-cooled microreactors [18]). Because UO_2, i.e., a ceramic material, has few free carriers, heat flow is dominated by phonons [19], making local bonding and vibrational amplitudes the primary controls of thermal conductivity. During irradiation in a nuclear reactor, fission deposits energy in the UO_2 fuel, produces point/extended defects (i.e., irradiation damage) and implanted fission products that scatter phonons, driving conductivity losses that can approach $\sim$ 70% over fuel lifetime [20]; conversely, irradiation-induced microstructures (e.g., high-burnup structure at the fuel pellet rim or at Pu-rich regions in case of (U, Pu)O_2 mixed-oxide fuel) can raise conductivity by draining defects to grain boundaries [21]. Capturing these effects requires models that resolve pair-specific structure and bond dynamics under irradiation and temperature extremes—the central targets of the measurement-and-theory framework presented here.

A central barrier to creating and validating models of bond dynamics is the lack of experimental observables that report directly on pair-specific dynamic structure. Extended x-ray absorption fine structure (EXAFS) fills this gap. Because the photoelectron core-hole state lives for 0.1–1 fs while atomic motions occur on 10–1000 fs timescales, an EXAFS measurement is effectively a weighted ensemble of snapshots of the local coordination around the absorbing atom, capturing many-body bond length distribution functions, including the partial pair distribution functions $g_{a-b}(r)$, where a is the absorbing element and b is a neighboring atom. Consequently, the EXAFS coordination numbers, interatomic distances, and Debye–Waller factors (DWFs), defined as mean-square relative displacements (MSRDs) of interatomic pairs, and higher cumulants provide direct measurements of pair-resolved local structure and dynamics that can be compared with theory. The DWF and MSRD denote the same quantity and are used interchangeably in this article as a nod to the EXAFS literature tradition, where both terms are frequently used.

In the conventional approach, the EXAFS is fit with an analytical EXAFS equation [22]:

$$\chi_i(k) = S_0^2\left(\frac{N_i f_i(k)}{kR_i^2}\right)e^{-2k^2\sigma_i^2}e^{-\frac{2R_i}{\lambda_i(k)}}\sin\left(2kR_i+\delta_i(k)\right), \quad (1)$$

where, for atoms within the ith shell from the absorbing atom, k is the photoelectron wave number, S_0^2 is the amplitude reduction factor, N_i is the coordination number, R_i is the effective half-path-length, σ_i^2 is the mean squared relative deviation in R (MSRD), and $\lambda(k)$, $f(k)$, and $\delta(k)$ are the photoelectron mean free path, scattering amplitude, and phase, respectively. The photoelectron scattering parameters are calculated via the Rehr-Albers approach under the muffin-tin approximation of the atomic potentials [23] with the FEFF software package (see, e.g., Ref. [24] for the latest version), while the remaining variables are obtained through least-squares fitting of the model to experimental data [25–27]. While the fitting approach is commonly used to study the static and/or dynamic disorder of materials via temperature-dependent analysis of σ_i^2, fitting experimental EXAFS data with Eq. (1) can be relatively less accurate for systems with strongly asymmetric static and or vibrational disorder [28–31]. The addition of cumulants may help account for bonding asymmetry, in general [32]. However, the effect of multimodal bonding distributions often present in crystalline and molten oxides and halides [29–31] on the validity of cumulant-based EXAFS analysis is generally not understood and has to be evaluated on a case-by-case basis. In addition, inverse approaches (given the spectrum, find structural and dynamic information) are fundamentally limited by the Shannon-Nyquist criterion [33]. Thus, we opt for a different, forward, approach to quantify the bonding dynamics by directly computing EXAFS using molecular dynamics (MD) simulations, a well-established strategy to benchmark interatomic potentials, often referred to as the MD-EXAFS method [34–37].

MD-EXAFS computes EXAFS spectra from MD trajectories, driven by a potential model for the Born-Oppenheimer potential, where the agreement between the theoretical and experimental EXAFS is the measure of the potential model's accuracy. Then, the MD trajectories are integrated to provide coordination numbers, distances, and MSRDs. This approach has been used successfully in many applications [34–36,38], but it is computationally intensive—especially for *ab initio* MD—and can be cumbersome for wide-temperature sweeps or open-ended potential-model screening.

Another approach, the dynamical-matrix Debye-Waller (DMDW) [39,40] method, avoids lengthy MD simulations and instead derives MSRDs and related quantities from the harmonic dynamical matrix, enabling rapid evaluation of pair dynamics across temperatures and configurations. When harmonic approximation holds, DMDW thus offers orders-of-magnitude speedups that are critical for exploring functional space (e.g., defect chemistries, interface terminations) and for coupling vibrational predictions to interfacial design, catalysis, and transport models. Critically, the DMDW method can be significantly more accurate than the conventional Einstein and Debye models [41,42]. In addition to the harmonic approximation constraint, as in MD, DMDW accuracy depends on the choices of underlying force constants and lattice constants, which, in turn, are determined by the potential model used. To fully exploit the speedup and accuracy of the DMDW method for modeling local bonding dynamics in metal oxides, those constraints and limitations must be analyzed.

Here we report a workflow that uses experimental EXAFS to validate interatomic potentials and predict temperature-dependent bond dynamics in UO_2 (Fig. 1). Theoretical EXAFS spectra calculated over the MD trajectory depend on the choice of the interatomic potentials employed in MD simulations. The agreement between the experimental (the ground truth) and MD-based EXAFS data validates the overall reliability of the MD-EXAFS calculations, including, importantly, the accuracy of the underlying interatomic potentials. The potentials are then used in the DMDW workflow to construct the dynamical matrix, and the projected density of

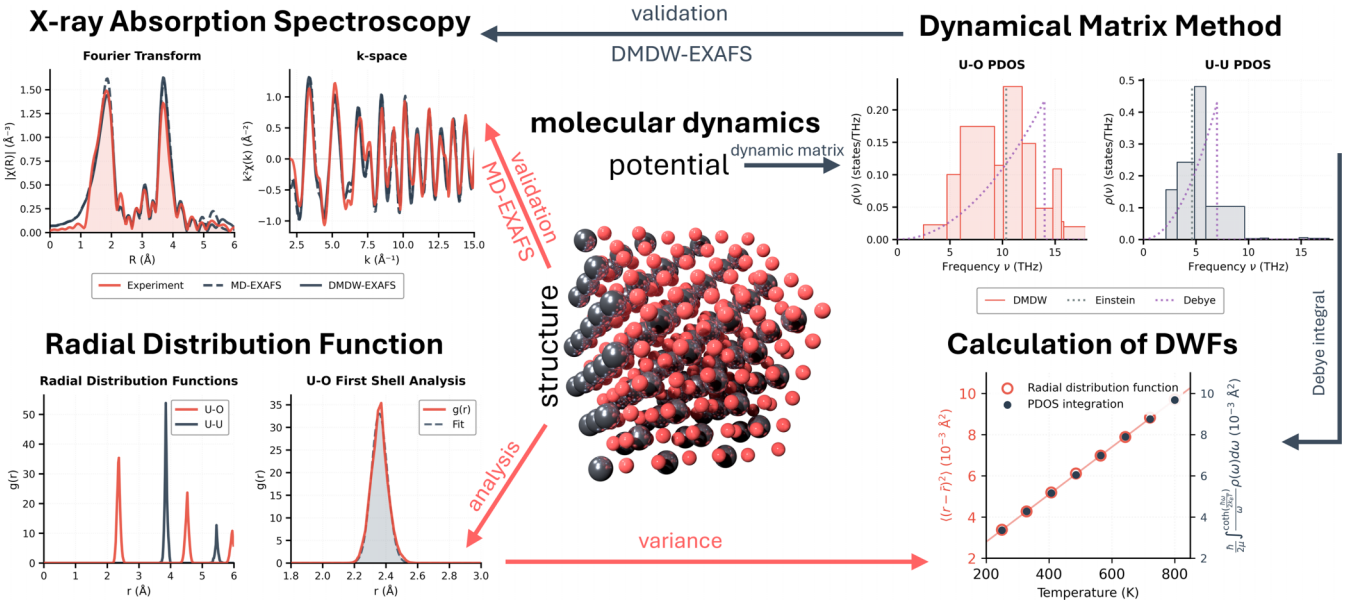

FIG. 1. A summary of our approach for validating and employing interatomic potentials to calculate Debye-Waller factors (DWFs) with the dynamical matrix Debye-Waller (DMDW) software. First, the interatomic potential is used to drive a molecular dynamics simulation, and a theoretical Extended X-ray Absorption Fine Structure (EXAFS) spectrum is calculated on the resulting MD trajectory and compared to an experimental EXAFS spectrum to validate the potential. After validation, the potential is used to construct the dynamical matrix, and subsequently the projected density of vibrational states via Lanczos Recursion, which is then integrated with the Debye integral to produce the DWFs. The DMDW-derived DWFs can also be used to construct a theoretical EXAFS spectrum (DMDW-EXAFS) for direct comparison with experiment. Finally, the partial radial distribution functions are calculated from the MD trajectory and integrated to obtain the DWFs. Black circles are U and red circles are O.

vibrational states is subsequently obtained via Lanczos recursion. As a frequently used characteristic of bond dynamics, DWFs can then be obtained from the usual Debye integrals over the phonon density of states (PDOS) (see below). To evaluate the accuracy in DWF predictions by the DMDW method, the MD-derived DWFs can also be calculated and compared with the DMDW-derived ones, closing the loop.

Two complementary theoretical EXAFS methods can be employed. The first, DMDW-EXAFS, constructs theoretical spectra directly from Debye-Waller factors computed via the dynamical matrix method, providing an independent validation of the interatomic potentials used. The DMDW-EXAFS method is limited for this purpose by the current limitations in EXAFS Eq. (1), which does not account for the disorder-induced variation of the temperature-dependent photoelectron scattering amplitudes and phases in multiple-scattering paths [43,44] and, hence, can be used at temperatures not too high above the Debye temperature of the oxides. The second, MD-EXAFS, calculates configuration-averaged spectra from molecular dynamics trajectories, naturally capturing anharmonic bonding disorder at a broad temperature range. With further application of the quasiharmonic approximation for the DMDW method, the two methods can be combined because they cover a broader temperature range than each of them independently, as demonstrated here.

In this work, we target UO_2 as a model actinide oxide. We use MD-EXAFS (and optional, alternative DMDW-EXAFS calculations could be used for this purpose, *vide infra*) to select a suitable potential for future use with DMDW to predict pair-specific bond dynamics. We show that the experimental EXAFS collected at 298, 773, 975, and 1171 K play a key role in the selection of appropriate interatomic force models used in both MD and DMDW. Within this calibrated framework, DMDW yields MSRDs that agree with those extracted from MD while enabling far faster evaluation and screening, thereby establishing a practical path to predictive bonding-dynamics calculations in UO_2 and, potentially, other oxides.

II. METHODS

A. Dynamical matrix Debye-Waller method

The temperature-dependent Debye-Waller factors, expressed as the MSRD (σ^2), were calculated from first principles using the DMDW code. DMDW provides a robust evaluation of σ^2 by integrating the projected PDOS, thereby avoiding the approximations inherent in simpler methods such as the correlated Debye or Einstein models.

The MSRD of a given atomic pair is obtained from the Debye integral [41]:

$$\sigma^2(T) = \frac{\hbar}{2\mu} \int \frac{1}{\omega} \coth\left(\frac{\hbar\omega}{2k_B T}\right) \rho(\omega) d\omega, \qquad (2)$$

where μ is the reduced mass of the atomic pair, T is the temperature, $\hbar$ is the reduced Planck's constant, k_{BT} is the Boltzmann constant, and $\rho(\omega)$ is the vibrational density of states projected onto the scattering path vector.

The DMDW code implements this calculation within the harmonic approximation. The essential input for the code is the dynamical matrix, which contains the interatomic force constants of the system.

From the provided dynamical matrix, DMDW employs the Lanczos algorithm to compute the projected PDOS as a

TABLE I. The mixtures and temperatures that lead to the formation of UO_2.

Temperature	Mixture[a]	History[b]
298 K	LiCl-KCl	298 → 773 → 298[c]
773 K	NaCl-$MgCl_2$	298 → 773[c]
975 K	NaCl	298 → 975[c]
1171 K	BN	298 → 1171[c]

[a]Salts mixed with UCl_3.
[b]Temperature in K.
[c]Temperature at which EXAFS was collected.

series of discrete poles (frequencies ω_i and weights w_i). This many-pole representation enables an accurate, direct calculation of the integral. The MSRD is then computed using the discretized form of Eq. (2):

$$\sigma^2(T) = \frac{\hbar}{2\mu} \sum_i \frac{w_i}{\omega_i} \coth\left(\frac{\hbar\omega_i}{2k_BT}\right). \tag{3}$$

This method has been shown to reproduce experimental Debye-Waller factors with high accuracy for a variety of molecular and crystalline systems [39,45]. For UO_2, 10 poles are sufficient for convergence.

The dynamical matrix for this work was calculated using two potential models: density functional theory (DFT) and an empirical interatomic potential (EIP). For DFT, three exchange-correlation functionals were employed: local density approximation (LDA), generalized gradient approximation as formulated by Perdew, Burke, and Ernzerhof (PBE) [46], and PBE revised for solids (PBEsol) [47]. The DFT calculations were carried out using the projector augmented-wave method [48,49], as implemented in the Vienna ab initio Simulation Package code [50,51]. To account for the strong electronic correlation in $5f$ electrons of uranium atoms, DFT+U with U= 4eV was used with the occupation matrix control method; the details of DFT calculations, including the supercell size, the cutoff energy, and k-point meshes, are provided in Refs. [52–54]. For EIP, two potentials were employed, the Meis-Chartier [55–57] potential and the Zhou potential [58], and the calculations were carried out using the General Utility Lattice Program (GULP) [59]. Finally, the dynamic matrices were computed via the lone irreducible derivative approach [54].

B. Experimental EXAFS

UO_2 was formed by oxidation of UCl_3 dissolved in chloride salt mixtures with different melting temperatures and measured 50 K above their melting points, as well as at room temperature after cooling from the melt (Table I). The formation of UO_2 in those salts will be described in our future work. The compositions of UCl_3 and salt mixtures were (1) UCl_3 diluted with BN, (2) NaCl (NaCl:UCl_3)=(0.5:0.5), (3) NaCl-$MgCl_2$ (NaCl:$MgCl_2$:UCl_3)=(0.545:0.364:0.091), and 4) LiCl-KCl (LiCl:KCl:UCl_3)=(0.592:0.318:0.09). In all cases, summarized in Table I, the UCl_3 oxidized to UO_2, as previously observed in [60].

The extended synthetic procedures for uranium(III) chloride salt were described in our previous study [61]. Briefly, uranyl nitrate was first converted to uranium trioxide by precipitating uranium peroxide with hydrogen peroxide, followed by thermal decomposition. Uranium trioxide was then chlorinated with hexachloropropene at elevated temperature to afford uranium tetrachloride. Finally, uranium(III) chloride was obtained by metallothermic reduction of UCl_4 with excess zinc metal under an inert atmosphere. To obtain salt mixtures, the as-prepared UCl_3 powder was combined in appropriate amounts with anhydrous NaCl/LiCl/KCl and $MgCl_2$ (99.99% purity, Aldrich-APL) in a glovebox to prepare the corresponding binary and ternary compositions. Following well-established procedures, these mixtures were fused at ∼ 1073 K under dynamic vacuum, then finely crushed and sealed in individual quartz ampoules under vacuum for shipment to the beamline. Due to the presence of oxygen in the initially prepared material, all samples oxidized upon melting, and *in situ* formation of solid UO_2 at high temperatures was detected, as observed previously [60].

EXAFS data were collected at the INE beamline [62] at the KIT Light Source (Karlsruhe Research Accelerator KARA, Karlsruhe, Germany), with 2.5 GeV and 150–170 mA as operating conditions in the storage ring. The INE beamline uses a Ge(422) double-crystal monochromator (DCM) and Rh-coated mirrors before (flat, cylindrically bent) and after (toroidal) the double crystal monochromator to collimate and focus the synchrotron beam, respectively, producing a spot size of 300 μm × 500 μm at the sample surface.

The data were collected simultaneously in transmission and fluorescence modes at the U L_3 edge at 773, 975, and 1171 K, respectively (with an uncertainty of around 10 K on the temperature reading). A custom high-temperature cell and furnace setup was used, as described in detail in [63]. The salts were inserted into predried BN containment cells as described in [58] under a dry atmosphere in an argon-filled glove box. The *in situ* high temperature measurements were performed under vacuum ∼ 10^{-4}–10^{-5} mbar). Before averaging, the XAS data (XANES and EXAFS) were aligned using metallic yttrium (K edge at 17038 eV) as a reference, placed between the second and third ionization chambers at the INE beamline, and measured simultaneously with the samples. Approximately 3–4 scans were merged, background-subtracted, and edge-step normalized for subsequent quantitative analysis. The data were Fourier transformed using a Hanning window over the k-range 2–15 $Å^{-1}$ (dk = 2 $Å^{-1}$) for 298 K and 2–9 $Å^{-1}$ for the high temperatures using ATHENA software [27].

To compare the state of UO_2 in the resultant samples with a bulk UO_2 reference, we used the room temperature data for the sample containing 9 mol % UCl_3 mixed with LiCl-KCl eutectic, heated to 773 K and then cooled to room temperature (Table I). In the Supplemental Material (SM) [64], Note 1 and Fig. 1 demonstrate good agreement between the XANES and EXAFS data for these two samples.

C. Molecular dynamics simulations

To select the appropriate interatomic potential for modeling the vibrational dynamics of UO_2, we employ the MD-EXAFS method, which assesses a potential by first using it to generate an MD trajectory, calculating the configuration-averaged EXAFS (i.e., over all absorbing atoms in the

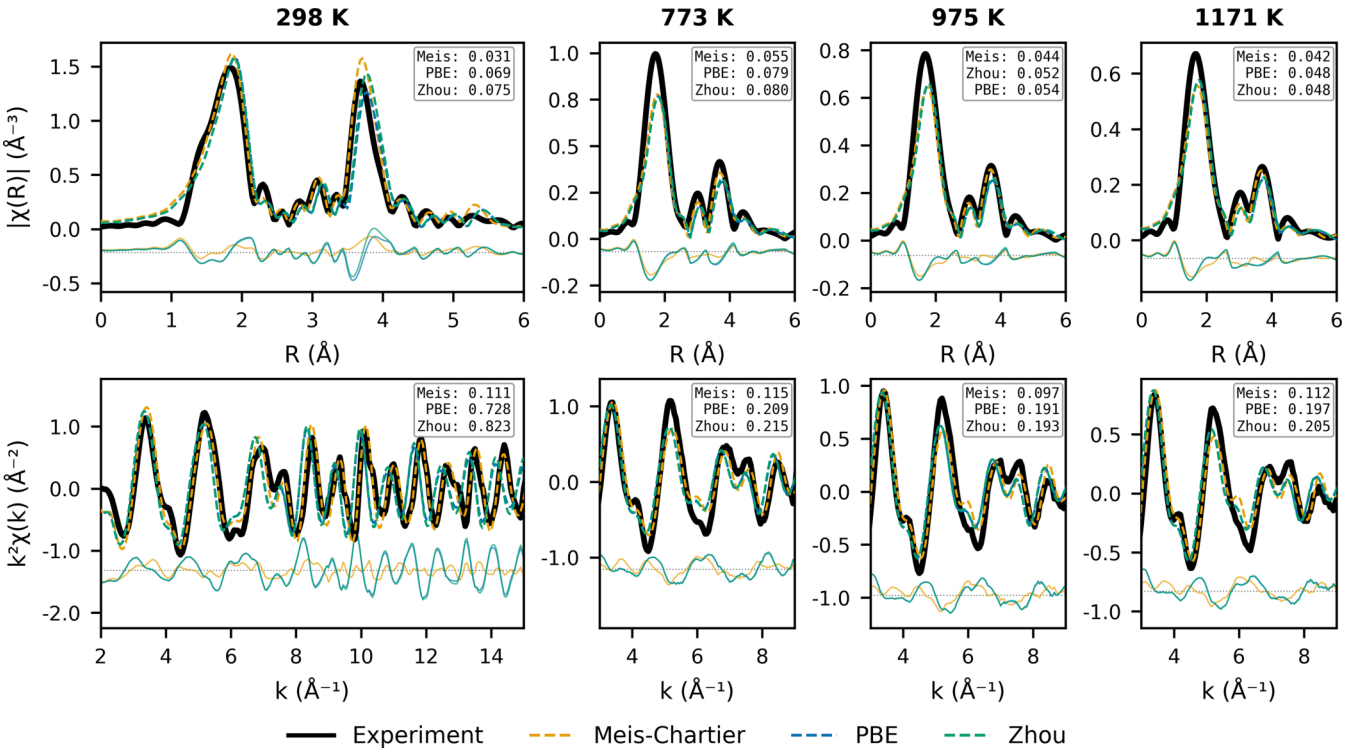

FIG. 2. Experimental (black, solid) k^2-weighted EXAFS (bottom row) and Fourier-transformed EXAFS (top row) compared to MD-EXAFS (Meis-Chartier: orange, dashed, PBE: blue, dashed, Zhou: green, dashed) at 298, 773, 975, and 1171 K. The Fourier transforms were performed between 2 and 9 Å^{-1} for 773–1171 K and from 2–15 Å^{-1} for 298 K, all with a Hanning window function of $dk = 2$ Å^{-1}. The experimental data were divided by the amplitude reduction factor (0.70), as explained in the text. *R* factors are included in the legend, and the residuals, compared to the experiment, are plotted under each dataset.

trajectory), and then comparing the theoretical and experimental EXAFS data. Here, we examine two promising potentials: an EIP- and PBE-based *ab initio* potential, yielding MD and *ab initio* MD (AIMD) simulations, respectively.

We chose the Meis-Chartier EIP [55–57] because it was previously validated at room temperature for simulating bulk UO_2 via MD-EXAFS [68]. The Meis-Chartier EIP accounts for electronic polarizability by treating both uranium and oxygen ions with a core-shell model. Short-range repulsive and van der Waals interactions are modeled using a Buckingham potential for O-O pairs and a Williams potential for O-U pairs, with a cutoff distance of 10.4 Å. Long-range electrostatic forces are handled by the Smooth Particle Mesh Ewald method.

Molecular dynamics simulations using the Meis-Chartier EIP were performed using the CP2K software package. The simulations were performed on a $3 \times 3 \times 3$ supercell of UO_2, corresponding to a cubic cell with a lattice parameter of 16.362 Å. The system was simulated in the canonical (NVT) ensemble, with the temperature maintained at 298, 773, 975, and 1171 K using a Nosé-Hoover chain thermostat. The equations of motion were integrated with a timestep of 1.0 fs for a total simulation time of 200 000 steps (200 ps) after a period of equilibration. For the highest-frequency phonon mode in UO_2 (∼20 THz), a 1.0 fs timestep provides 50 sampling points per vibrational period.

The AIMD simulations were performed using the VASP code [50,51] with the PBE functional. DFT+U with $U = 4$ eV and spin–orbit coupling was included. A $3 \times 3 \times 3$ supercell of UO_2, corresponding to a cubic cell with a lattice parameter of 16.638 Å, was employed, and only the Γ point was used for Brillouin-zone sampling. The simulations were carried out in the NVT ensemble using a Nosé–Hoover thermostat at 298, 773, 975, and 1171 K. A time step of 1.0 fs was used, and a total simulation time of 20 000 steps (20 ps) was collected after an initial equilibration period. An on-the-fly machine-learning force field [69] as implemented in VASP was used to accelerate the AIMD simulations; this approach trains a surrogate interatomic potential adaptively during the simulation to reduce the number of explicit DFT evaluations while maintaining *ab initio* accuracy.

D. MD-EXAFS

Before a comparison can be made, the experimental EXAFS is corrected for the passive electron reduction factor, which is often assumed to be 1 in theoretical simulations. Here, we obtained the value of the reduction factor (0.70) by fitting the UO_2 EXAFS data at room temperature using standard methods (SM Note 1, SM Fig. 2). Then, the experimental EXAFS spectra were divided by this factor.

EXAFS was calculated for each uranium absorber with FEFF 8.5 Lite [23,70,71] and averaged over the trajectory. Full details of MD-EXAFS simulations are in SM Note 2.

For the MD and AIMD trajectories, radial distribution functions were created for U-U and U-O pairs and averaged over the respective trajectories. Integration and direct statistics were calculated on the RDFs between the first nearest

neighbor U-O and U-U peaks to provide the area (coordination number), mean (interatomic distance), variance (MSRD, σ^2), and skew (C_3) for each bond.

In UO_2, the lattice parameter change is less than 1% from 298 K to 1171 K, as measured experimentally [72], therefore, NVT simulations with a fixed lattice constant of 5.454 Å were performed at experimental temperatures of 298, 773, 975, and 1171 K. From the converged part of each trajectory, 1000 frames were selected, and the U L_3 EXAFS was calculated for 10 random U atoms per frame. The resulting 10 000 EXAFS calculations were averaged. Full details of using FEFF8.5L [70]. For details of the EXAFS calculations, see SM Note 2.

E. DMDW-EXAFS

To directly compare the DMDW predictions with experiment, theoretical EXAFS spectra were calculated using FEFF10 with temperature-dependent Debye-Waller factors supplied by the DMDW method. The dynamical matrix, computed from the Meis-Chartier EIP using GULP, was provided to FEFF via the DEBYE card. The absorbing atom was chosen as the U atom closest to the center of the supercell to maximize the number of complete scattering paths within the cutoff radius (RPATH = 6.5 Å), yielding 35 paths. This approach treats atomic vibrations within the harmonic approximation, producing σ^2 values that account for correlated thermal motion along each scattering path but do not capture anharmonic contributions to the pair distribution function.

III. RESULTS

A. DWFs via MD-EXAFS

Following the MD-EXAFS method, the Meis-Chartier [68], Zhou [58], and PBE models were used to drive MD and AIMD simulations, respectively. Thus, we can select the best of the three and use it to quantify the temperature-dependent disorder in the experimental data at 298, 773, 975, and 1171 K.

The calculated and experimental EXAFS are shown in Fig. 2, revealing good agreement for all three potential models. However, the Meis-Chartier interatomic potential shows better agreement with the experimental data at all temperatures, particularly in the peak positions, due to the overestimation of the equilibrium lattice constants in PBE+U for which the other two potentials are based. The agreement beyond the first coordination shell ($\sim$ 2.5 Å) is also encouraging, as it shows that the Meis-Chartier EIP captures higher-order correlations, boosting confidence in our ability to quantify the static and dynamic structure in UO_2. Thus, we conclude that the simpler EIP is sufficient for modeling UO_2 over the temperature range and use it in the remaining steps of our analysis.

The resulting MD trajectories were analyzed by first extracting the pair distribution functions for U-U ($g_{U-U}(r)$) and U-O ($g_{U-O}(r)$) pairs up to 6 Å (the approximate range that the photoelectron probes around the absorbing atom). Descriptive statistics of the first nearest-neighbor contributions to $g_{U-O}(r)$, from 1.8 to 3.2 Å, and $g_{U-U}(r)$, from 3.2 to 4.5 Å, were calculated with the following approach. For absorbing atoms A and neighboring atoms B with partial

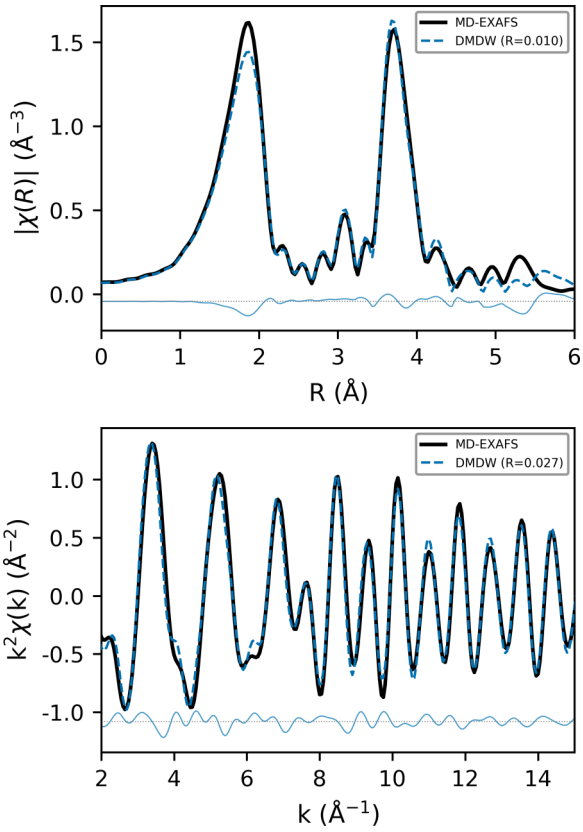

FIG. 3. MD-EXAFS (black, solid) k^2-weighted (bottom row) and Fourier-transformed EXAFS (top row) compared to DMDW-EXAFS (blue, dashed) at 298 K. The Fourier transform was performed between 2–15 Å^{-1} with a Hanning window function of $dk = 2$ Å^{-1}. The R factor (legend) and the residual (under each dataset) are compared to MD-EXAFS.

radial distribution $g_{A-B}(r)$, the integrated area, mean, variance, and skew calculated for the first coordination shell between r_{min} and r_{max} are equivalent to the first-nearest-neighbor coordination number (CN_{A-B}), interatomic distance (R_{A-B}), Debye-Waller-Factor/MSRD (σ^2_{A-B}), and third cumulant (C_3^{A-B}), respectively, defined by the following;

$$CN_{A-B} = 4\pi\rho_B \int_{r_{min}}^{r_{max}} g_{A-B}(r) r^2 dr, \quad \rho_B = \frac{N_B}{V}, \tag{4}$$

$$R_{A-B} = \frac{\int_{r_{min}}^{r_{max}} r g_{A-B}(r) dr}{\int_{r_{min}}^{r_{max}} g_{A-B}(r) dr}, \tag{5}$$

$$\sigma^2_{A-B} = \frac{\int_{r_{min}}^{r_{max}} (r - R_{A-B})^2 g_{A-B}(r) dr}{\int_{r_{min}}^{r_{max}} g_{A-B}(r) dr}, \tag{6}$$

$$C_3^{A-B} = \frac{\int_{r_{min}}^{r_{max}} (r - R_{A-B})^3 g_{A-B}(r) dr}{\int_{r_{min}}^{r_{max}} g_{A-B}(r) dr}, \tag{7}$$

where ρ_B is the number density of B atoms (N_B) in the simulation box of volume V. These parameters are summarized in SM Note 3 and SM Fig. 3.

In addition, parametric Gaussian and Skew models were used to fit $g_{U-O}(r)$ and $g_{U-U}(r)$ from 1.8 to 3.2 Å and 3.2 to 4.5 Å, respectively, to determine which model better represents the bond length distribution—details in SM Note 3, SM Fig. 3, and SM Table I. At all temperatures, the U-O

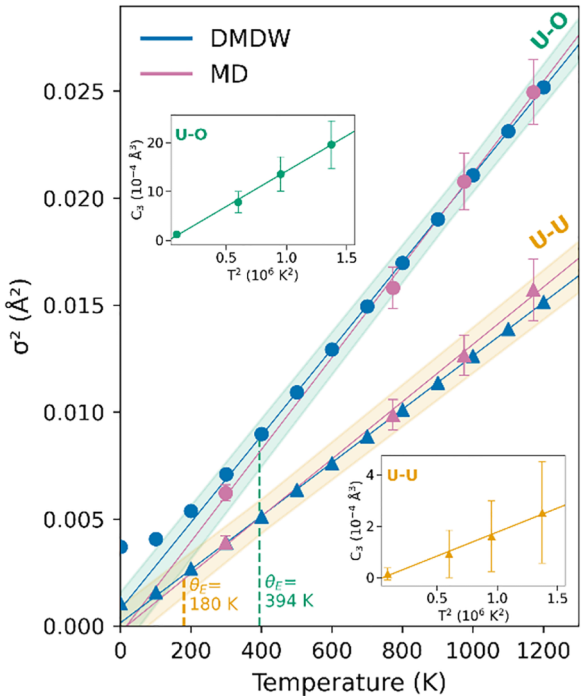

FIG. 4. Debye-Waller factors (DWFs, σ^2) vs temperature for U-O (circles, teal-shaded zone) and U-U (triangles, orange-shaded zone) bonding calculated by DMDW (blue) and molecular dynamics (pink), both using the Meis-Chartier empirical potential. The error bars are the standard deviation of the MSRD calculated over 1000 frames. Vertical dashed lines indicate the effective Einstein temperatures for U-O (∼ 394 K) and U-U (∼ 180 K). The insets show C_3 values obtained from the Meis-Chartier molecular dynamics trajectories, which scale linearly with T^2 as expected from the Frenkel-Rehr model [32].

bond length distribution is better fit by the skew model, while U-U is fit equally well by the Gaussian and skew model (SM Table I).

B. DMDW-EXAFS versus MD-EXAFS

To validate the DMDW approach independently of the MD simulations, we constructed theoretical EXAFS spectra directly from the DMDW-derived Debye-Waller factors and compared them to the experimental data. Figure 3 shows the DMDW-EXAFS and Meis-Chartier MD-EXAFS at 298 K. The purely harmonic DMDW-EXAFS reproduces the MD-EXAFS well at room temperature, where both anharmonic effects and angular bonding disorder are small. The DMDW-EXAFS calculation requires minutes of CPU time compared to days for a full MD-EXAFS calculation, demonstrating that the DMDW method can replace the MD method for reproducing EXAFS oscillations (for the relatively low temperature range, vide supra).

C. DMDW calculations of MSRDs

MSRDs were calculated with DMDW between 300 and 1200 K using the validated Meis-Chartier EIP with the equilibrium lattice constant of 5.454 Å. Additionally, to illustrate the effects of lattice constants and potentials, MSRDs were calculated using the Zhou EIP, PBE, PBEsol, and LDA functionals. In all cases, displayed in SM Fig. 5 and SM Table 2, changes in the lattice constant manifest as a change in the slope of the MSRD vs temperature curve, as expected, with the difference between functionals being due to over- or underbinding.

D. MSRD: MD versus DMDW predictions

The MSRDs of the Meis-Chartier U-O and U-U radial distribution functions, integrated between 1.8 and 3.2 Å and 3.2 and 4.5 Å, respectively, are compared to the Meis-Chartier DMDW outputs in Fig. 4. Overall, the two methods are in good agreement, but systematic pair-specific deviations are observed. For U-O, DMDW predicts larger σ^2 than MD at temperatures below ca. 298 K; the two methods are in agreement, within error bars, up to high temperatures. For U-U, the methods agree, within the error bars, at all temperatures.

The third cumulant C_3, also shown in Fig. 4, increases with temperature for both pairs, with U-O exhibiting substantially larger values than U-U, consistent with the greater anharmonicity of the U-O bond. The change in C_3 is proportional to the square of the temperature, as predicted by the Frenkel-Rehr model [32], thus further validating the MD simulations. The effective Einstein temperatures, provided by DMDW, for the U-O (394 K) and U-U (180 K) pairs, indicated by dashed lines in Fig. 4, demarcate the quantum and classical regimes for each pair. The physical origins of these trends are analyzed in the Discussion.

IV. DISCUSSION

This work demonstrates a robust workflow for calculating pair-specific bond dynamics in UO_2. By first validating an empirical interatomic potential against experimental EXAFS data, we replace computationally intensive MD simulations with much faster and more accurate (in the low temperature range, where classical MD simulations do not account for zero point motion) DMDW calculations. Interatomic potential validation can be performed by comparing either MD-EXAFS or DMDW-EXAFS spectra (taking into account the limitations of the temperatures, unique for each method, as demonstrated in this work) with experimental data (Fig. 3). The central finding is that the DMDW method, when supplied with a validated potential, predicts mean-square relative displacements of atomic pairs (U-O and U-U, as demonstrated here) and takes into account low temperature, quantum effects. The experimental EXAFS data play an essential role in selecting the interatomic potential. The agreement between the calculated EXAFS spectra and experimental data (Fig. 2) confirms that the Meis-Chartier potential accurately captures the atomic structure and dynamics of UO_2 from 298 K to 1171 K. This agreement extends beyond the first coordination shell, indicating that the potential correctly models many-body correlations, which is essential for predicting bulk material properties. Furthermore, the analysis of the MD trajectories reveals that the U-O bond length distribution is non-Gaussian (skewed), a feature that conventional EXAFS fitting struggles to capture but is naturally handled by the MD-EXAFS approach. This reinforces the need for methods that can account

for the true shape of atomic pair distributions, especially in systems with significant thermal or static disorder.

As demonstrated in SM Fig. 5, the calculated DWFs are sensitive to the choice of potential model and lattice constant. Different *ab initio* functionals produce different slopes in the MSRD vs temperature curves, reflecting differences in bond stiffness (i.e., over- or underbinding), while changes in the lattice constant cause a uniform shift in slope. For UO_2, among the employed *ab initio* functionals (PBE, LDA, and PBEsol), PBE provides the best predictions for DWFs, consistent with previous studies indicating that PBE offers better predictions for phonon spectra than LDA [52]. Similarly, the recently developed Zhou potential also provides accurate predictions for DWFs. The sensitivity of DWFs to different potential models underscores the necessity of experimental validation; without it, selecting a force model would be arbitrary and likely lead to inaccurate predictions of vibrational dynamics.

The DMDW-EXAFS results (Fig. 3) demonstrate that the computationally efficient DMDW pathway reproduces the experimental spectra with R factors comparable to full MD-EXAFS. Because DMDW-EXAFS achieves this accuracy at a fraction of the computational cost, it could itself serve as the potential-selection tool in future applications, eliminating the need for MD-EXAFS for this purpose for systems in the low-temperature regime, where angular bonding disorder, hampering the ability of DMDW-EXAFS to reproduce the photoelectron scattering properties, is relatively low.

The comparison of DMDW and MD values of σ^2 in Fig. 4 reveals pair-specific trends that reflect two distinct physical effects: nuclear quantum statistics and lattice anharmonicity. These effects are encoded in the two methods' different treatments of nuclear motion. Classical MD treats nuclei dynamics according to Newton's equations. Due to the equipartition theorem (each vibrational mode receives energy k_BT), σ^2 vanishes linearly as $T \to 0$. DMDW, by contrast, evaluates Eq. (2) with full quantum statistics via the $\coth(\hbar\omega/2k_BT)$ kernel, which yields a finite zero-point contribution $\sigma^2 \to \hbar/(2\mu\omega)$ at $T = 0$ [32,39]. Importantly, this distinction is independent of whether the underlying potential is empirical or *ab initio*—the potential determines the vibrational frequencies, while the coth kernel determines how those frequencies are thermally populated [39,41].

For U-O pairs, DMDW predicts larger σ^2 than MD at 298 K, with the two methods converging and crossing over near 800 K, above which MD exceeds DMDW (Fig. 4). The low-temperature offset is a direct consequence of quantum zero-point motion. The U-O stretching modes correspond to high-frequency optical phonons, giving an effective Einstein temperature of 394 K (dashed line, Fig. 4). At 298 K, the system is well below this characteristic temperature, placing the U-O pair in the quantum regime where zero-point motion contributes significantly to σ^2. Classical MD, which enforces equipartition, underestimates σ^2 in this regime. As the temperature increases, both methods converge toward the classical limit. However, a second effect emerges at elevated temperatures: the U-O bond potential is anharmonic, as evidenced by the skewed bond length distribution and the growing third cumulant C_3 (SM Figs. 3 and 4). This anharmonicity introduces positive corrections to σ^2 that are captured by MD—which samples the full anharmonic potential energy surface —but not by DMDW, which operates within the harmonic approximation. We also note that this is only a fraction of the total expected anharmonicity, given that the MD simulations are NVT. In reality, the total anharmonicity would be larger due to thermal expansion of the cell. The approximate crossover near 800 K, while within the statistical uncertainties of the MD-derived values, is consistent with the expected competition between the quantum zero-point contribution (which favors DMDW > MD at low T) and the anharmonic correction (which favors MD > DMDW at high T). We note that the precise crossover temperature cannot be determined from the current data due to the overlap of error bars, but the trend is physically motivated and consistent with the effective Einstein temperature of the U-O pair ($\sim$ 394 K). In future work, we recommend using DMDW in the quasiharmonic approximation, e.g., by calculating a dynamical matrix at each temperature, which has been shown to capture anharmonicity relative to purely harmonic calculations [39,73].

For U-U pairs, a different balance is presented. The relevant vibrational modes are low-frequency acoustic modes, yielding an effective Einstein temperature of 180 K (dashed line, Fig. 4). At 298 K, the system is well above this temperature, and quantum corrections to σ^2 are negligible. Accordingly, DMDW and MD agree well at low temperatures. As temperature increases, however, MD yields progressively larger σ^2 than DMDW, consistent with a growing anharmonic contribution. The third cumulant C_3 for U-U also increases with temperature (Fig. 4), confirming that anharmonicity, rather than a quantum-classical discrepancy, drives the divergence.

Together, the two pairs bracket the regime of DMDW validity. The U-O pair isolates the quantum zero-point effect at low temperature and the anharmonic effect at high temperature, with a visible crossover between the two regimes. The U-U pair, where quantum effects are negligible, isolates the anharmonic contribution. This pair-specific analysis demonstrates that DMDW is quantitatively reliable when anharmonic corrections to σ^2 remain small relative to the harmonic contribution, and that it provides a more physically complete description than classical MD at temperatures below or near the effective Einstein temperature of the relevant modes. For applications requiring only σ^2 within the harmonic regime, DMDW is both computationally efficient and more accurate than classical MD at moderate temperatures. For systems with stronger anharmonicity, or when higher-order cumulants (C_3 and beyond) are needed, i.e., at relatively high temperatures, complementary MD simulations remain a useful additional method. Alternatively, the deployment of DMDW within the quasiharmonic approximation may also be promising for investigating other anharmonic effects, for example, those caused by defects, as demonstrated in a recent work [74], provided that relevant structural models are available. The primary advantage of the DMDW approach is computational efficiency: it offers orders-of-magnitude speedup over MD, enabling rapid screening of different defect configurations, compositions, or interfaces while retaining the quantum-statistical treatment of nuclear motion that classical MD lacks.

V. SUMMARY AND OUTLOOK

In this work, we demonstrate a robust and efficient workflow for predicting atomic bond dynamics in UO_2. We show that the computationally rapid DMDW method produces Debye-Waller factors in good agreement with those from computationally intensive MD simulations, provided both use the same validated interatomic potential. Pair-specific deviations between the two methods are traced to two fundamental effects: the quantum zero-point contribution to σ^2, which DMDW captures through the $\coth(\hbar\omega/2k_BT)$ kernel but classical MD does not, and bond anharmonicity, which MD captures by sampling the full potential energy surface, while DMDW, operating within the harmonic approximation, does not. For the U-O pair, these effects compete, producing a crossover near 800 K; for the U-U pair, where quantum corrections are negligible, the anharmonic contribution dominates. Therefore, if an interatomic potential is first validated against experimental data using MD-EXAFS or DMDW-EXAFS at one or more temperatures, it can then be used within the DMDW framework to model the material's dynamics over a broad temperature range without the need for further MD simulations, with the additional advantage that DMDW provides a more physically accurate treatment of nuclear quantum effects than classical MD. at moderate temperatures. This workflow provides a practical path forward for future studies, enabling the high-throughput screening of complex systems.

ACKNOWLEDGMENTS

This work was primarily supported as part of the Molten Salts in Extreme Environments Energy Frontier Research Center, funded by the U.S. Department of Energy (DOE) Office of Science, Office of Basic Energy Sciences. BNL, INL and ORNL are operated under DOE Contracts No. DE-SC0012704, No. DE-AC07-05ID14517, and No. DE-AC05-00OR22725, respectively. N.M. acknowledges support from the U.S. Department of Energy, Office of Basic Energy Sciences Award No. DE-SC0022199. N.M. is supported by the Joint Photon Sciences Institute at Stony Brook University. S.Z. is supported by the Center for Thermal Energy Transport under Irradiation, an Energy Frontier Research Center funded by the U.S. Department of Energy Office of Basic Energy Sciences. F.D.V. is supported by Co-ACCESS, part of the SUNCAT Center for Interface Science and Catalysis, provided by the DOE BES, Chemical Sciences, Geosciences, and Biosciences Division, with computational support from NERSC, a DOE Office of Science User Facility, under Contract No. DE-AC02-05CH11231. This research made use of the resources of the High Performance Computing Center at Idaho National Laboratory, which is supported by the Office of Nuclear Energy of the U.S. Department of Energy and the Nuclear Science User Facilities under Contract No. DE-AC07-05ID14517. The authors thank Stony Brook Research Computing and Cyberinfrastructure and the Institute for Advanced Computational Science at Stony Brook University for access to the high-performance SeaWulf computing system, which was made possible by grants from the National Science Foundation (Awards No. 1531492 and No. 2215987) and matching funds from the Empire State Development's Division of Science, Technology and Innovation (NYSTAR) program (Contract No. C210148). We finally acknowledge the KIT Light Source for the provision of instruments at the INE beamline of the Institute for Nuclear Waste Disposal (KIT-INE) and thank the Institute for Beam Physics and Technology (KIT-IBPT) for the operation of the KARA storage ring (Karlsruhe Research Accelerator). A.I.F. and F.D.V. are grateful to Prof. J. J. Rehr (University of Washington) for introducing them to the study of vibrational dynamics through EXAFS analysis.

DATA AVAILABILITY

The data that support the findings of this article are openly available [75].

[1] J. Mannhart and D. G. Schlom, Oxide interfaces—an opportunity for electronics, Science **327**, 1607 (2010).

[2] S. Sahoo, K. Y. Wickramathilaka, E. Njeri, D. Silva, and S. L. Suib, A review on transition metal oxides in catalysis, Frontiers in Chemistry **12**, 1374878 (2024).

[3] Y. G. Zhu, J. Y. Wang, S. B. Patel, C. R. Li, A. R. Head, J. A. Boscoboinik, and G. W. Zhou, Tuning the surface reactivity of oxides by peroxide species, Proc. Nat. Acad. Sci. USA **120**, e2215189120 (2023).

[4] H. Wang, M. Kottwitz, N. Rui, S. D. Senanayake, N. Marinkovic, Y. Li, R. G. Nuzzo, and A. I. Frenkel, Aliovalent doping of CeO_2 improves the stability of atomically dispersed Pt, ACS Appl. Mater. Interfaces **13**, 52736 (2021).

[5] Y. Li, M. Kottwitz, J. L. Vincent, M. J. Enright, Z. Liu, L. Zhang, J. Huang, S. D. Senanayake, W.-C. D. Yang, P. A. Crozier, *et al.*, Dynamic structure of active sites in ceria-supported Pt catalysts for the water gas shift reaction, Nat. Commun. **12**, 914 (2021).

[6] G. Li, D. N. Zakharov, T. Hu, Y. Yu, I. Waluyo, A. Hunt, A. R. Head, and J. A. Boscoboinik, Tracking the dynamics of catalytic Pt/CeO_2 active sites during water-gas-shift reaction, Commun. Mater. **5**, 133 (2024).

[7] B. Li, Y. Hao, X. Shao, H. Tang, T. Wang, J. Zhu, and S. Yan, Synthesis of hierarchically porous metal oxides and Au/TiO_2 nanohybrids for photodegradation of organic dye and catalytic reduction of 4-nitrophenol, J. Catal. **329**, 368 (2015).

[8] S. O. Owalude, I. T. Olowookere, I. Perera, H. S. Khanna, E. Njeri, X. Huang, A. G. Meguerdichian, H.-T. O. Ayilara, and S. L. Suib, Photocatalytic degradation of orange II dye via high pore volume polymorph zirconium-doped titania under visible light irradiation, Appl. Surf. Sci. **616**, 156452 (2023).

[9] A. Bhuin, S. Udayakumar, J. Gopalarethinam, D. Mukherjee, K. Girigoswami, C. Ponraj, and S. Sarkar, Photocatalytic degradation of antibiotics and antimicrobial and anticancer activities of two-dimensional ZnO nanosheets, Sci. Rep. **14**, 10406 (2024).

[10] K. Zhu, X. Li, Y. Chen, Y. Huang, Z. Yang, G. Guan, and K. Yan, Recent advances on the spherical metal oxides for sustainable degradation of antibiotics, Coord. Chem. Rev. **510**, 215813 (2024).

[11] S. Lin, H. Huang, T. Ma, and Y. Zhang, Photocatalytic oxygen evolution from water splitting, Adv. Sci. **8**, 2002458 (2021).

[12] K. Takanabe, Photocatalytic water splitting: Quantitative approaches toward photocatalyst by design, ACS Catalysis **7**, 8006 (2017).

[13] M. Kumar, B. Meena, P. Subramanyam, D. Suryakala, and C. Subrahmanyam, Recent trends in photoelectrochemical water splitting: The role of cocatalysts, npg Asia Mater. **14**, 88 (2022).

[14] T. Li, W. Zeng, and Z. Wang, Quasi-one-dimensional metal-oxide-based heterostructural gas-sensing materials: A review, Sens. Actuators B **221**, 1570 (2015).

[15] A. Kumar, A. Sanger, A. Kumar, and R. Chandra, Fast response ammonia sensors based on TiO_2 and NiO nanostructured bilayer thin films, RSC Adv. **6**, 77636 (2016).

[16] M. S. S. Danish, A. Bhattacharya, D. Stepanova, A. Mikhaylov, M. L. Grilli, M. Khosravy, and T. Senjyu, A systematic review of metal oxide applications for energy and environmental sustainability, Metals **10**, 1604 (2020).

[17] M. G. Sensoy, R. W. Carpick, D. J. Srolovitz, and A. M. Rappe, Manipulating the electrical properties of conductive substoichiometric titanium oxides, Phys. Rev. B **109**, 064106 (2024).

[18] D. L. Doyle, E. M. Duchnowski, J. R. Trelewicz, and N. R. Brown, Ceramic composite inert matrix fuel forms in high-temperature gas-cooled microreactors, Nucl. Sci. Eng. **199**, 2234 (2025).

[19] C. Ronchi, M. Sheindlin, M. Musella, and G. J. Hyland, Thermal conductivity of uranium dioxide up to 2900 K from simultaneous measurement of the heat capacity and thermal diffusivity, J. Appl. Phys. **85**, 776 (1999).

[20] C. Ronchi, M. Sheindlin, D. Staicu, and M. Kinoshita, Effect of burn-up on the thermal conductivity of uranium dioxide up to 100.000 MWdt−1, J. Nucl. Mater. **327**, 58 (2004).

[21] D. H. Hurley, A. El-Azab, M. S. Bryan, M. W. D. Cooper, C. A. Dennett, K. Gofryk, L. F. He, M. Khafizov, G. H. Lander, M. E. Manley, *et al.*, Thermal energy transport in oxide nuclear fuel, Chem. Rev. **122**, 3711 (2022).

[22] D. E. Sayers, E. A. Stern, and F. W. Lytle, New technique for investigating noncrystalline structures: Fourier analysis of the extended x-ray—absorption fine structure, Phys. Rev. Lett. **27**, 1204 (1971).

[23] J. J. Rehr and R. C. Albers, Scattering-matrix formulation of curved-wave multiple-scattering theory: Application to x-ray-absorption fine structure, Phys. Rev. B **41**, 8139 (1990).

[24] J. J. Kas, F. D. Vila, C. D. Pemmaraju, T. S. Tan, and J. J. Rehr, Advanced calculations of x-ray spectroscopies with FEFF10 and Corvus, J. Synchrotron Radiat. **28**, 1801 (2021).

[25] M. Newville, T. Stensitzki, D. B. Allen, and A. Ingargiola, LMFIT: Non-linear least-square minimization and curve-fitting for python, Zenodo, 2015, https://dx.doi.org/10.5281/zenodo.598352.

[26] M. Newville, Larch: An analysis package for XAFS and related spectroscopies, J. Phys. Conf. Ser. **430**, 012007 (2013).

[27] B. Ravel, and M. Newville, ATHENA, HEPHAESTUS: Data analysis for X-ray absorption spectroscopy using IFEFFIT, J. Synchrotron Radiat. **12**, 537 (2005).

[28] A. Yevick and A. I. Frenkel, Effects of surface disorder on EXAFS modeling of metallic clusters, Phys. Rev. B **81**, 115451 (2010).

[29] S. K. Gill, J. Huang, J. Mausz, R. Gakhar, S. Roy, F. Vila, M. Topsakal, W. C. Phillips, B. Layne, S. Mahurin, *et al.*, Connections between the Speciation and Solubility of Ni(II) and Co(II) in Molten $ZnCl_2$, J. Phys. Chem. B **124**, 1253 (2020).

[30] S. Roy, Y. Liu, M. Topsakal, E. Dias, R. Gakhar, W. C. Phillips, J. F. Wishart, D. Leshchev, P. Halstenberg, S. Dai, *et al.*, A holistic approach for elucidating local structure, dynamics, and speciation in molten salts with high structural disorder, J. Am. Chem. Soc. **143**, 15298 (2021).

[31] K. Zheng, N. Patra, N. Marcella, A. S. Ivanov, J. F. Wishart, A. R. Ballesteros, R. Gakhar, S. Dai, S. Roy, V. Bryantsev, *et al.*, X-ray absorption studies of local structure of dilute ionic species in molten salts, Chem.–Methods **5**, e202400097 (2025).

[32] A. I. Frenkel and J. J. Rehr, Thermal expansion and x-ray-absorption fine-structure cumulants, Phys. Rev. B **48**, 585 (1993).

[33] J. J. Rehr and R. C. Albers, Theoretical approaches to x-ray absorption fine structure, Rev. Mod. Phys. **72**, 621 (2000).

[34] A. Kuzmin and R. A. Evarestov, Quantum mechanics–molecular dynamics approach to the interpretation of x-ray absorption spectra, J. Phys. Condens. Matter **21**, 055401 (2009).

[35] B. J. Palmer, D. M. Pfund, and J. L. Fulton, Direct modeling of EXAFS spectra from molecular dynamics simulations, J. Phys. Chem. **100**, 13393 (1996).

[36] S. W. T. Price, N. Zonias, C.-K. Skylaris, T. I. Hyde, B. Ravel, and A. E. Russell, Fitting EXAFS data using molecular dynamics outputs and a histogram approach, Phys. Rev. B **85**, 075439 (2012).

[37] L. A. Mistryukova, N. P. Kryuchkov, V. N. Mantsevich, A. V. Sapelkin, and S. O. Yurchenko, Interpolation method for crystals with many-body interactions, Phys. Rev. B **104**, 054108 (2021).

[38] F. Vila, J. J. Rehr, J. Kas, R. G. Nuzzo, and A. I. Frenkel, Dynamic structure in supported Pt nanoclusters: Real-time density functional theory and x-ray spectroscopy simulations, Phys. Rev. B **78**, 121404(R) (2008).

[39] F. D. Vila, J. J. Rehr, H. H. Rossner, and H. J. Krappe, Theoretical x-ray absorption Debye-Waller factors, Phys. Rev. B **76**, 014301 (2007).

[40] A. V. Poiarkova and J. J. Rehr, Recursion method for multiple-scattering XAFS Debye-Waller factors, J. Synchrotron Radiat. **6**, 313 (1999).

[41] E. Sevillano, H. Meuth, and J. J. Rehr, Extended x-ray absorption fine structure Debye-Waller factors. I. Monatomic crystals, Phys. Rev. B **20**, 4908 (1979).

[42] N. Van Hung and J. J. Rehr, Anharmonic correlated Einstein-model Debye-Waller factors, Phys. Rev. B **56**, 43 (1997).

[43] A. Frenkel, E. A. Stern, A. Voronel, M. Qian, and M. Newville, Buckled crystalline structure of mixed ionic salts, Phys. Rev. Lett. **71**, 3485 (1993).

[44] A. Frenkel, E. A. Stern, A. Voronel, M. Qian, and M. Newville, Solving the structure of disordered mixed salts, Phys. Rev. B **49**, 11662 (1994).

[45] A. Smerigan, S. Biswas, F. D. Vila, J. Y. Hong, J. Perez-Aguilar, A. S. Hoffman, L. Greenlee, R. B. Getman, and S. R. Bare, Aqueous structure of lanthanide-EDTA coordination complexes

determined by a combined DFT/EXAFS approach, Inorganic Chemistry **62**, 14523 (2023).
[46] J. P. Perdew, K. Burke, and M. Ernzerhof, Generalized gradient approximation made simple, Phys. Rev. Lett. **77**, 3865 (1996).
[47] J. P. Perdew, A. Ruzsinszky, G. I. Csonka, O. A. Vydrov, G. E. Scuseria, L. A. Constantin, X. Zhou, and K. Burke, Restoring the density-gradient expansion for exchange in solids and surfaces, Phys. Rev. Lett. **100**, 136406 (2008).
[48] P. E. Blöchl, Projector augmented-wave method, Phys. Rev. B **50**, 17953 (1994).
[49] G. Kresse and D. Joubert, From ultrasoft pseudopotentials to the projector augmented-wave method, Phys. Rev. B **59**, 1758 (1999).
[50] G. Kresse and J. Hafner, *Ab initio* molecular dynamics for liquid metals, Phys. Rev. B **47**, 558 (1993).
[51] G. Kresse and J. Furthmüller, Efficient iterative schemes for *ab initio* total-energy calculations using a plane-wave basis set, Phys. Rev. B **54**, 11169 (1996).
[52] S. Zhou, H. Ma, E. Xiao, K. Gofryk, C. Jiang, M. E. Manley, D. H. Hurley, and C. A. Marianetti, Capturing the ground state of uranium dioxide from first principles: Crystal distortion, magnetic structure, and phonons, Phys. Rev. B **106**, 125134 (2022).
[53] S. Zhou, E. Xiao, H. Ma, K. Gofryk, C. Jiang, M. E. Manley, D. H. Hurley, and C. A. Marianetti, Phonon thermal transport in UO_2 via self-consistent perturbation theory, Phys. Rev. Lett. **132**, 106502 (2024).
[54] L. Fu, M. Kornbluth, Z. Cheng, and C. A. Marianetti, Group theoretical approach to computing phonons and their interactions, Phys. Rev. B **100**, 014303 (2019).
[55] C. Meis and A. Chartier, Calculation of the threshold displacement energies in UO_2 using ionic potentials, J. Nucl. Mater. **341**, 25 (2005).
[56] F. Devynck, M. Iannuzzi, and M. Krack, Frenkel pair recombinations in UO_2: Importance of explicit description of polarizability in core-shell molecular dynamics simulations, Phys. Rev. B **85**, 184103 (2012).
[57] M. Krack, Atomistic simulation of nuclear fuels, MRS Online Proceed. Library **1383**, 19 (2011).
[58] S. Zhou, C. Jiang, E. Xiao, S. Bandi, M. W. D. Cooper, M. Jin, D. H. Hurley, M. Khafizov, and C. A. Marianetti, Parameterizing empirical interatomic potentials for predicting thermophysical properties via an irreducible derivative approach: The case of ThO_2 and UO_2, J. Phys. Condens. Matter **37**, 255901 (2025).
[59] J. D. Gale, GULP: A computer program for the symmetry-adapted simulation of solids, J. Chem. Soc. Faraday Transactions **93**, 629 (1997).
[60] B. W. Tuffy, N. R. Birkner, J. Schorne-Pinto, R. C. Davis, A. M. Mofrad, C. M. Dixon, M. Aziziha, M. S. Christian, T. J. Lynch, M. T. Bartlett, *et al.*, Identification and decomposition of uranium oxychloride phases in oxygen-exposed UCl_3 salt compositions, J. Phys. Chem. B **127**, 6091 (2023).
[61] D. S. Maltsev, D. M. Driscoll, Y. Zhang, J. C. Neuefeind, B. Reinhart, C. Agca, D. Ray, P. W. Halstenberg, M. Aziziha, J. Schorne-Pinto, *et al.*, Transient covalency in molten uranium(III) chloride, J. Am. Chem. Soc. **146**, 21220 (2024).
[62] J. Rothe, S. Butorin, K. Dardenne, M. A. Denecke, B. Kienzler, M. Löble, V. Metz, A. Seibert, M. Steppert, T. Vitova, *et al.*, The INE-Beamline for actinide science at ANKA, Rev. Sci. Instrum. **83**, 043105 (2012).
[63] A. L. Smith, M. N. Verleg, J. Vlieland, D. de Haas, J. A. Ocadiz-Flores, P. Martin, J. Rothe, K. Dardenne, M. Salanne, A. E. Gheribi, *et al.*, *In situ* high-temperature EXAFS measurements on radioactive and air-sensitive molten salt materials, J. Synchrotron Radiat. **26**, 124 (2019).
[64] See Supplemental Material at http://link.aps.org/supplemental/10.1103/l3lr-qhdz for Notes 1–4, Figs. 1–5, Tables 1 and 2, and Eqs. (1)–(13), which includes Refs. [65–67].
[65] M. Idiri, T. Le Bihan, S. Heathman, and J. Rebizant, Behavior of actinide dioxides under pressure: UO_2 and ThO_2, Phys. Rev. B **70**, 014113 (2004).
[66] S. V. Sukhomlinov and M. H. Müser, Determination of accurate, mean bond lengths from radial distribution functions, J. Chem. Phys. **146**, 024506 (2017).
[67] A. Azzalini, A class of distributions which includes the normal ones, Scand. J. Stat. **12**, 171 (1985).
[68] D. Bocharov, M. Chollet, M. Krack, J. Bertsch, D. Grolimund, M. Martin, A. Kuzmin, J. Purans, and E. Kotomin, Analysis of the U L_3-edge X-ray absorption spectra in UO_2 using molecular dynamics simulations, Prog. Nucl. Energy **94**, 187 (2017).
[69] R. Jinnouchi, F. Karsai, and G. Kresse, On-the-fly machine learning force field generation: Application to melting points, Phys. Rev. B **100**, 014105 (2019).
[70] A. L. Ankudinov, B. Ravel, J. J. Rehr, and S. D. Conradson, Real-space multiple-scattering calculation and interpretation of x-ray-absorption near-edge structure, Phys. Rev. B **58**, 7565 (1998).
[71] B. Ravel and M. Newville, feff85exafs: Initial release, Zenodo, 2015, https://dx.doi.org/10.5281/zenodo.20629.
[72] J. K. Fink, Thermophysical properties of uranium dioxide, J. Nucl. Mater. **279**, 1 (2000).
[73] F. D. Vila, S. T. Hayashi, and J. J. Rehr, Efficient calculation of the negative thermal expansion in ZrW_2O_8, Front. Chem. **6** 2018 (2018).
[74] Y. Chen, R. Rana, T. Sours, F. D. Vila, S. Cao, T. Blum, J. Hong, A. S. Hoffman, C.-Y. Fang, Z. Huang, *et al.*, A theory-guided x-ray absorption spectroscopy approach for identifying active sites in atomically dispersed transition-metal catalysts, J. Am. Chem. Soc. **143**, 20144 (2021).
[75] N. Marcella, S. Zhou, F. D. Vila, N. Patra, A. Kuzmin, D. S. Maltsev, A. S. Ivanov, S. Dai, R. Gakhar, K. Dardenne, *et al.*, Reproduction data for Fast and accurate calculation of EXAFS Debye-Waller factors in UO_2 using the dynamical matrix method [Data set], Zenodo, 2026, https://doi.org/10.5281/zenodo.18674004.

Correction: The source information for Ref. [31] was incorrect and has been fixed.